# Coseismic fault lubrication by viscous deformation

Giacomo Pozzi, Nicola de Paola, Stefan B Nielsen, Robert E Holdsworth, Telemaco Tesei, Manuel Thieme, Sylvie Demouchy

Author copy of the final (peer-reviewed) version
Article published in Nature Geoscience in May 2021.
https://doi.org/10.1038/s41561-021-00747-8

# Coseismic fault lubrication by viscous deformation

**Giacomo Pozzi** [1]✉, **Nicola De Paola** [1]✉, **Stefan B. Nielsen** [1], Robert E. Holdsworth [1], Telemaco Tesei [2], Manuel Thieme [3] and Sylvie Demouchy [3]

Despite the hazard posed by earthquakes, we still lack fundamental understanding of the processes that control fault lubrication behind a propagating rupture front and enhance ground acceleration. Laboratory experiments show that fault materials dramatically weaken when sheared at seismic velocities ( $>0.1\,m\,s^{-1}$). Several mechanisms, triggered by shear heating, have been proposed to explain the coseismic weakening of faults, but none of these mechanisms can account for experimental and seismological evidence of weakening. Here we show that, in laboratory experiments, weakening correlates with local temperatures attained during seismic slip in simulated faults for diverse rock-forming minerals. The fault strength evolves according to a simple, material-dependent Arrhenius-type law. Microstructures support this observation by showing the development of a principal slip zone with textures typical of sub-solidus viscous flow. We show evidence that viscous deformation (at either sub- or super-solidus temperatures) is an important, widespread and quantifiable coseismic lubrication process. The operation of these highly effective fault lubrication processes means that more energy is then available for rupture propagation and the radiation of hazardous seismic waves.

Earthquakes are among the deadliest natural disasters, with statistics showing a global death toll of >50,000 per year in the period 2000–2016[1]. Despite their impact on society, there is still a lack of fundamental understanding about earthquake constitutive behaviour. During seismic events, part of the mechanical energy stored in the stressed rocks is dissipated by frictional heating along the fault, causing the local temperatures to rise[2,3]. This promotes the onset of thermally activated weakening mechanisms that help to reduce the shear strength[4–6] in the fast-sliding portion of the fault, behind the rupture front[2,3]. Efficient lubrication means that more elastic energy can be transferred to the rupture tip, promoting earthquake propagation and enhancing the dissipation of energy into hazardous seismic waves[7,8]. Therefore, the characterization and quantification of weakening mechanisms associated with the faulting process are crucial issues in seismology and fault mechanics[7].

In the past decades, several weakening mechanisms have been proposed on the basis of theoretical models and results of laboratory friction experiments that simulate high-velocity seismic slip in rocks. Among these, the flash-heating model[5,9] is important thanks to its general formulation. However, the flash-weakening mechanism relates to the concept of load-bearing asperities and does not consider their evolution during slip. With increasing slip, pressures and temperatures, flash heating is likely to evolve to other thermally controlled processes[4,5] such as frictional melting[10–12] (common in silicate rocks) or thermal pressurization[13,14] (due to fluids initially present in the fault or released by thermal decomposition processes). Other weakening mechanisms proposed include powder lubrication[15,16], silica gel lubrication[17] and thermal decomposition[18]. More recently, an alternative weakening mechanism has been described in experiments using carbonate gouges, where coseismic deformation is accommodated by ductile creep mechanisms[19–22]. Despite this wide range of weakening mechanisms described in the literature, the processes involved in fault lubrication are still not fully understood. In particular, there is no quantitative model for fault lubrication during earthquake slip[4] in fine-grained granular material (fault gouges) that can account for both experimental and seismological observations and be fully supported by microstructural studies (melt lubrication aside[10,12,23]).

In this article, we investigate coseismic weakening mechanisms in several rock-forming minerals by integrating mechanical data from shear experiments on powders at high velocity ($v > 0.1\,m\,s^{-1}$) with microstructural analyses. The results, summarized in the following, show that the strengths of the analysed materials follow a common temperature-dependent law and develop microstructures consistent with viscous deformation mechanisms.

## Shear experiments at seismic velocity

We shear powders (grain size 63–90 µm) of a range of silicate and non-silicate, anhydrous rock-forming minerals (experimental procedure as in Pozzi et al.[22] and references therein[20,21]). Specifically, we tested carbonate (calcite[20] and dolomite[24,25]), sulfate (anhydrite[26]), halide (halite[27]) and silicate (olivine[28,29]) powders, which are commonly used as analogues for a range of natural fault gouges[30]. These minerals do not produce frictional melts (apart from halite) and do not contain structural water, hydroxyl or hydrogen. The testing materials and conditions were chosen to diminish the efficiency of flash-heating processes[5,31] (by using fine-grained powders) and to exclude the contribution of fluid-driven mechanisms to fault weakening[10,16,20,21,25].

A normal stress of $\sigma_n = 25$ MPa (20 MPa for olivine) was applied to the gouges and held constant throughout the tests. The samples were then sheared at room temperature and humidity at different seismic velocities (0.28–1.4 $m\,s^{-1}$) for ~1 m of total slip. This amount of slip is enough to produce weakening, but still not large enough to produce substantial thermal decomposition, frictional melting and other physical changes in the rocks[20,25].

[1]Department of Earth Sciences, Rock Mechanics Laboratory, University of Durham, Durham, UK. [2]Department of Geosciences, University of Padova, Padova, Italy. [3]Geosciences Montpellier, CNRS and Université de Montpellier, UMR5243, Montpellier, France. ✉e-mail: giacomo.pozzi@ingv.it; nicola.de-paola@durham.ac.uk

Author copy of the final (peer-reviewed) version
Article published in Nature Geoscience in May 2021.
https://doi.org/10.1038/s41561-021-00747-8

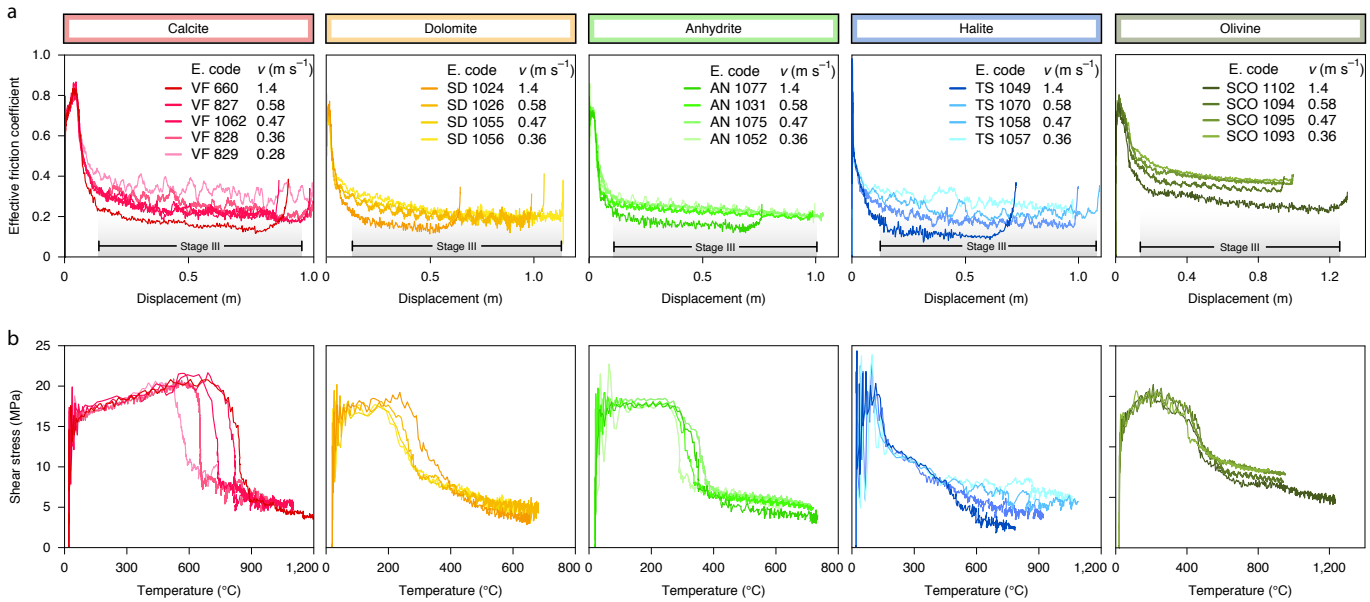


Fig. 1 | Mechanical data. a, $\mu^*$ evolving with displacement during Stages I–IV (see text for details). During Stage III, $\mu^*$ values are lower in experiments run at higher velocities. Each experiment terminates with partial re-strengthening during deceleration to arrest b, Shear stress as a function of calculated temperature (up to Stage III). Note that the Stage III mechanical data of calcite, dolomite and anhydrite—and with good approximation for halite and olivine—collapse onto a single material-characteristic curve. Halite curves overlap up to a temperature of ~440 °C. E. code, alphanumerical experiment code.

For each experiment, the effective friction coefficient $\mu^*$ (the measured ratio between shear and normal stress, which is not dependent on any particular deformation mechanism) follows a classic weakening profile[21] (Fig. 1a). Initial slip hardening in the Byerlee's range (Stage I; $\mu^*=0.6–0.9$)—almost absent in halite—is followed by an abrupt decay of fault strength to low friction values (Stage II; $\mu^*<0.4$). Friction then remains low during shearing at constant velocity, showing a slow decay with slip (Stage III in Fig. 1a). Partial re-strengthening is observed during the final deceleration and arrest of slip (Stage IV). The bulk temperature in the principal slip zone (PSZ) cannot be measured directly and is obtained using an equation for one-dimensional thermal diffusion[13] (Fig. 1b and Methods).

## Microstructures and deformation mechanisms

After each run, samples were carefully recovered and cross sections of the most deformed parts were prepared for microstructural analysis (Fig. 2f and Supplementary Figs. 3–11). In all experiments, we observe a PSZ with finite thickness of a few tens of microns (Fig. 2) that shows marked textural differences with the surrounding materials. The PSZs are characterized by fine-grained polygonal aggregates with extremely low porosity, fairly homogeneous grain size and oblique foliation[21] (Fig. 2). Little overprinting of microstructures due to late- and/or post-deformation annealing (Supplementary Section II) or by local embrittlement during stage IV[21] (white arrows in Fig. 2a–e) is expected in our experiments.

At high magnifications, within the PSZs, grains show low aspect ratio[22] (on an average, nearly equant), display diamond shapes, quadruple junctions, narrow gaps and numerous grain boundaries aligned with the shear direction (Supplementary Fig. 12a–d and Supplementary Section III). These textures are compatible with mechanisms of neighbour switching that are typical of grain-boundary sliding[32,33] (GBS, Fig. 3e). Microstructural analysis in calcite experiments suggests diffusion-accommodated GBS[19,20,22], although we do not exclude dislocation-accommodated GBS for the other materials. Transmission electron microscope imaging in both calcite and olivine shows that PSZ grains contain dislocations (Fig. 3f–i), dislocation walls and subgrains (regions bounded by dislocation walls, Fig. 3f,i), indicative of dislocation creep (DC) mechanisms. Notably, oblique foliation (Fig. 2) development is compatible with both GBS and DC mechanisms[34,35].

These observations extend recent results of high-velocity experiments in calcite gouges showing that deformation during Stage III slip is controlled by a combination of grain-size-sensitive (GBS) and grain-size-insensitive (DC) creep mechanisms[19–22]. DC limits the grain growth in the PSZ[36–38] (by formation of subgrains, Fig. 3f), while diffusion-assisted GBS could be instrumental in explaining the measured low stress[19–22,38]. Microstructural observations from all other materials tested here also support the hypothesis that coseismic deformation is accommodated by viscous processes at sub-melting temperatures.

## Arrhenius-type flow law describes coseismic fault strength

Microstructural analyses suggest that the PSZ accommodates almost all of the shear deformation and maintains constant thickness throughout Stage III[21], meaning that its strain rate is nearly constant. During Stage III, for each material, the natural logarithm of shear stress ($\tau$) versus the inverse values of calculated temperature (Fig. 4a) shows—to a good approximation—a linear trend with specific slope (thick lines in Fig. 4b).

Exponential regression allows computation of the dependence of fault strength $\tau$ on temperature $T$ during Stage III, which follows the equation

$$\ln \tau = A\frac{1}{T} + B \quad (1)$$

where $A$ and $B$ are best-fit constants. The specific best-fit equations of each material-dependent curve are reported in Fig. 4.

Ductile creep mechanisms share a similar exponential relationship following the general Arrhenius-type constitutive equation[39]

$$\dot{\gamma} = C\,\frac{\tau^n}{D^m}e^{-\frac{Q}{RT}} \quad (2)$$

Author copy of the final (peer-reviewed) version
Article published in Nature Geoscience in May 2021.
https://doi.org/10.1038/s41561-021-00747-8

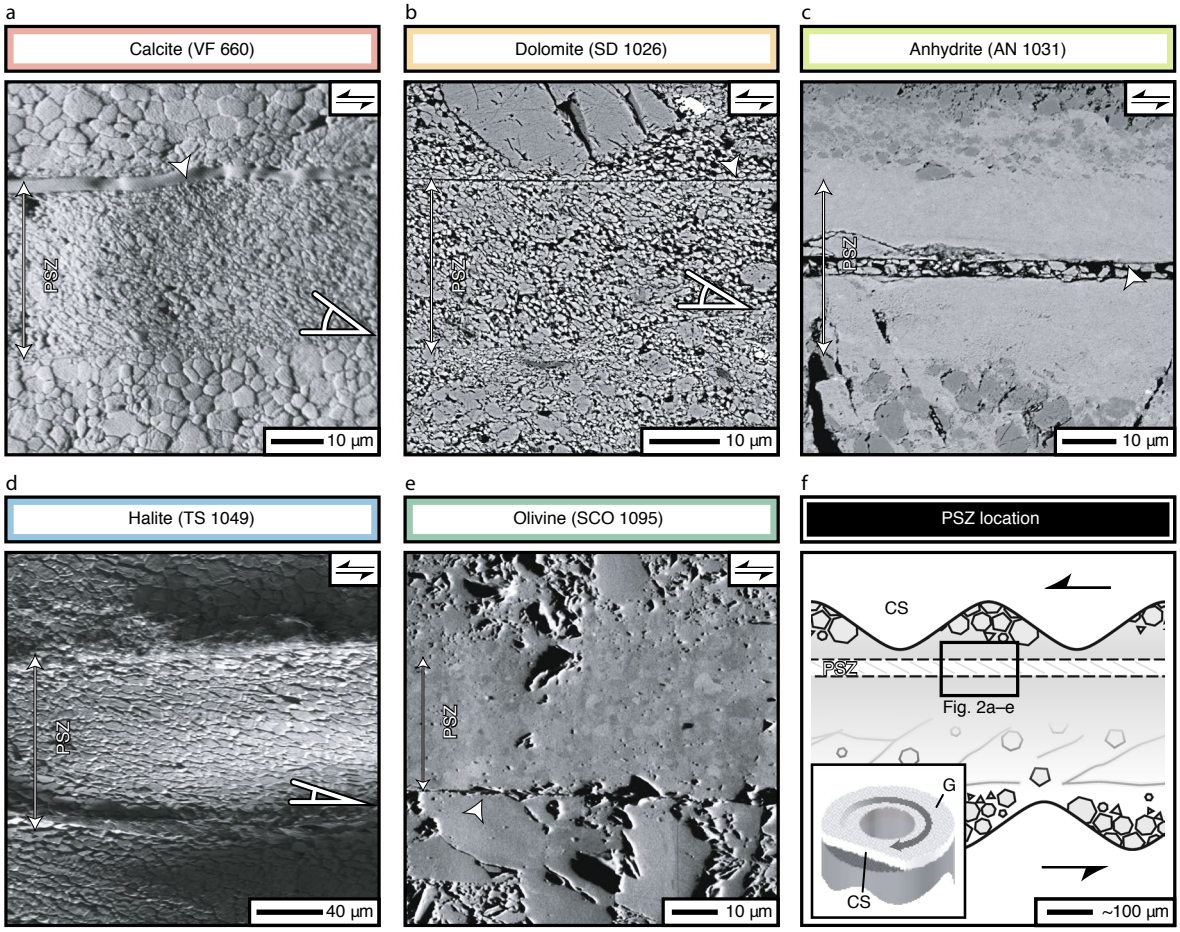


Fig. 2 | Microstructures. a–e, Forescattered ( a,e) and backscattered ( b–d) scanning electron microscope images of sample PSZs in polished cross sections cut parallel to the slip direction. PSZs are composed by polygonal aggregates with low porosity and fairly homogeneous grain size (close-ups in Fig3). In a, b and d an oblique (white angle) ultramylonitic foliation is visible. White arrows highlight local brittle overprint of Stage IV[21,22]. f, A schematic cross section of the samples. The rectangle shows the location of the microstructures in panels a–e. Inset of panel f shows the approximate location of the cross section (CS) with respect to the whole sheared gouge sample (G). The round arrow shows the shear direction.

where $\dot{\gamma}$ is the shear strain rate, $C^*$ is a pre-exponential constant, $D$ is the mean grain size, $n$ and $m$ are the stress and grain-size exponents, respectively, $Q$ is the activation energy and $R$ is the gas constant. Equation (2) can be rearranged[40] to:

$$\ln \tau = \left[\frac{Q}{nR}\right]\frac{1}{T} + \left[\frac{1}{n}\ln\left(\dot{\gamma}\frac{D^m}{C}\right)\right] \quad (3)$$

which is directly comparable to equation (1).

The PSZ grains were simultaneously affected by GBS (Fig. 3a) and DC mechanisms (Fig. 3c). Our observations confirm the hypotheses formulated by Ashby and Verrall[32] in their pioneering work on the flow of superplastic alloys, which predicted that GBS and DC are likely to occur simultaneously in nature. The slope $A$ in equation (1) is controlled primarily by the ratio of activation energy $Q$ and stress exponent $n$, normalized by the gas constant $R$ (equation 3); hence, it is not the expression of a single deformation mechanism.

The combination of mechanical data and microstructural observations suggests that the flow rate in the PSZ is dominated by the most effective mechanism, which in calcite is arguably some type of diffusion-accommodated GBS[19–22]. DC is the mechanism that limits the grain growth in the PSZ[36–38] of calcite samples (for example, by subgrain rotation[22]), and it might become the dominant deformation mechanism in other materials.

It is worth noting that the ratio $A = Q/nR$ obtained for all tested materials is substantially lower than that obtained from previous studies performed at lower strain, sub-seismic strain rate and coarser grain size, for both grain-size-sensitive and grain-size-insensitive creep (Supplementary Section VI). Such previous studies accept that best-fit parameters of flow laws evolve with increasing strain and can be considered constant only for limited ranges of strain[36–38,41–43]. Looking forwards, our results highlight the need for further research to improve our understanding of the physics of deformation processes across the transition from low to high strain and from sub-seismic to seismic strain rates.

The comparison between equations (1) and (3) shows that the intercept $B$ is controlled primarily by strain rate, grain size, grain-size exponent $m$ and pre-exponential factor $C^*$.

The linear fit of experimental data and microstructural observations point to a grain-size-dependent rheology in which fault strength is controlled mainly by temperature according to an Arrhenius-type law, while the interplay of different creep mechanisms adjusts to the evolving conditions.

During Stage III, olivine aggregates show a change of dependence of fault stress to temperature (change of slope, $A$ term in equation 1) at values above $T \approx 900$ °C (Fig. 4b). Such a temperature threshold corresponds to a homologous temperature ($T/T_m$) of ~0.57, where the melting temperature of forsterite olivine ($Fo_{90}$) is

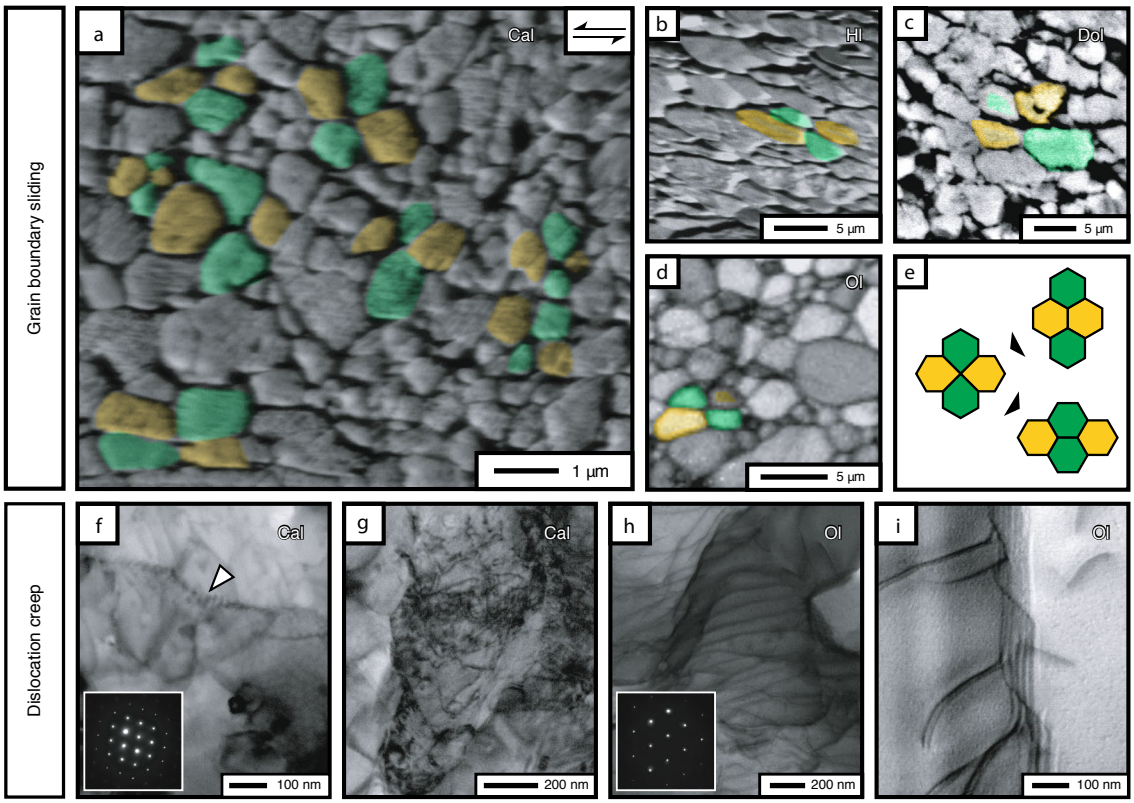


Fig. 3 | Deformation mechanisms. a–d, Scanning electron microscope images of the grains within the PSZs. The textures were captured using forescattered electron (a), backscattered electron ( b,c) and electron backscatter diffraction band contrast ( d) imaging. Sense of shear is top-to-the-left. Polygonal grains show fairly equant to slightly elongated shapes. Grains are diamond shaped and commonly display quadruple junctions (sets of four grains highlighted in green and yellow), boundaries aligned with the shear direction and narrow gapse, Sketches of neighbour-switching processes typical of GBS[32]; grains are coloured in green and yellow for comparison witha–d. f–i, Transmission electron images of the PSZ acquired in scanning mode show dislocations, dislocation walls (white arrow in f) and subgrains (≤200 nm in size, f). The PSZ is formed by crystalline material as shown by the diffraction pattern (insets in f and h). Cal, calcite; Hl, halite; Dol, dolomite; Ol, olivine.

$T_m = 1{,}765\,°C$[28]. This might suggest a change of the involved deformation mechanisms and reduced material strength, which is consistent with previous studies reporting faster rheological weakening in olivine[44] when $T > 0.6T_m$.

## Implications for coseismic weakening mechanisms

We have shown that coseismic weakening observed in a range of different minerals is plausibly achieved through viscous deformation along faults. We therefore propose that localization of deformation into thin PSZs and the associated weakening are likely controlled by a balance between heat production (by shear heating) and dissipation (by thermal diffusion and endothermic processes)[4,23,45]. The PSZ system will evolve towards its steady state by the minimization of viscous strain energy when a stable temperature profile is established across the slip zone at larger amounts of slip[4]. This rheological evolution is similar to that known for coseismic frictional melts where the molten layer properties are controlled by the heat balance across the fault[23]. Notably, the melt viscosity that controls the shear resistance of the fault (friction) is also controlled by a well-constrained Arrhenius-type dependency to temperature[23,46]. For comparison, see the linear slope in the inset of Fig. 4b, which was measured during weakening by melt lubrication of high-velocity shear experiments of gabbro[23].

We also note that, in the alternative model of flash heating[5,13], bulk weakening is achieved through the temperature rise at the asperity scale, which causes plastic softening and/or melting of contacts[5,12]. The mechanisms of flash heating are thus likely to also be viscous in nature and not mutually exclusive with our findings. The bulk behaviour of the fault is a function of the distribution and dimensions of asperities, which influence the local energy budget. In conclusion, the difference between flash heating and viscous deformation in a PSZ might simply be related to the scale of observation.

The similarity of the processes involved during coseismic slip is in good agreement with the observed ubiquity of weakening documented at seismic velocities across a wide range of fault materials[4]. Therefore, we propose that coseismic weakening by viscous processes at either sub- (coseismic ultramylonites[22]) or super-solidus (frictional melt[10,12,23]) temperatures is more widespread than previously thought. These mechanisms obey a simple Arrhenius-type dependency to temperature, whose thermodynamic parameters can be potentially determined through experimental investigation. Our results offer an alternative, quantitative viewpoint of fault strength-controlling processes and provide a new perspective on the role of ductile processes active along faults at seismic strain rates.

## Online content

Any methods, additional references, Nature Research reporting summaries, source data, extended data, supplementary information, acknowledgements, peer review information; details of author contributions and competing interests; and statements of

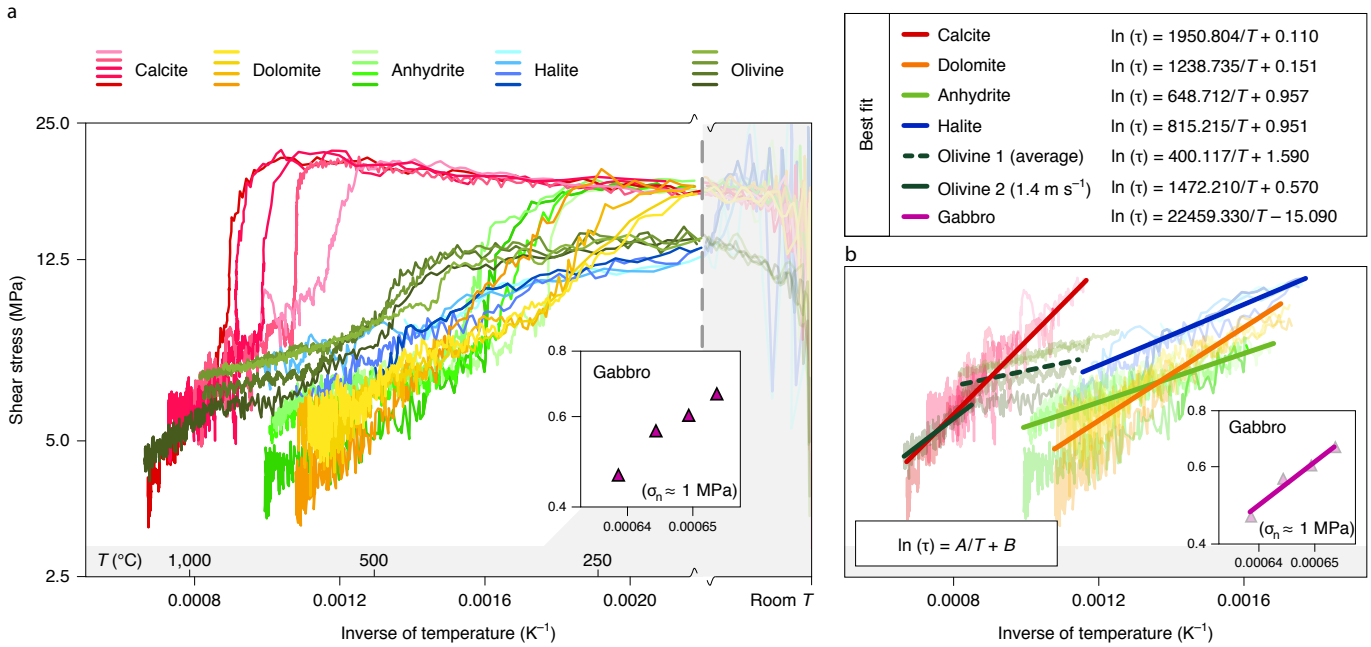


Fig. 4 | Mechanical data in Arrhenius space. a, Data presented in Fig. 1 are rearranged here in an Arrhenius space (natural logarithm of shear stress as a function of the inverse of calculated temperature). b, When the fault strength is weak, the mechanical data of each experiment fall on a material-dependent, characteristic straight line. The best-fit equation is shown on the graph for each material. The insets show mechanical data of Stage III of melt lubrication experiments performed on gabbro; data from Nielsen et al.[23]. $\sigma_n$, normal stress; $\tau$, shear stress; T, temperature.

data and code availability are available at https://doi.org/10.1038/s41561-021-00747-8.

Received: 18 July 2019; Accepted: 30 March 2021;
Published online: 17 May 2021

## References

1. *Global Death Toll Due to Earthquakes from 2000 to 2015* (Statista Research Department, 2016); https://www.statista.com/statistics/263108/global-death-toll-due-to-earthquakes-since-2000/
2. Kanamori, H. & Rivera, L. in *Earthquakes: Radiated Energy and the Physics of Faulting* (eds Abercrombie, R. et al.) 3–13 (AGU, 2006).
3. Nielsen, S. et al. G: fracture energy, friction and dissipation in earthquakes. *J. Seismol.* **20**, 1187–1205 (2016).
4. Di Toro, G. et al. Fault lubrication during earthquakes. *Nature* **471**, 494–499 (2011).
5. Goldsby, D. L. & Tullis, T. E. Flash heating leads to low frictional strength of crustal rocks at earthquake slip rates. *Science* **334**, 216–218 (2011).
6. Hirose, T. & Shimamoto, T. Growth of molten zone as a mechanism of slip weakening of simulated faults in gabbro during frictional melting. *J. Geophys. Res.* **110**, B05202 (2005).
7. Scholz, C. H. & Christopher, H. *The Mechanics of Earthquakes and Faulting* (Cambridge Univ. Press, 2002).
8. Noda, H. & Lapusta, N. Stable creeping fault segments can become destructive as a result of dynamic weakening. *Nature* **493**, 518–521 (2013).
9. Rice, J. R. Flash heating at asperity contacts and rate-dependent friction. *Eos Trans. AGU* **80**, F6811 (1999).
10. Di Toro, G., Hirose, T., Nielsen, S., Pennacchioni, G. & Shimamoto, T. Natural and experimental evidence of melt lubrication of faults during earthquakes. *Science* **311**, 647–649 (2006).
11. Spray, J. G. Frictional melting processes in planetary materials: from hypervelocity impact to earthquakes. *Annu. Rev. Earth Planet. Sci.* **38**, 221–254 (2010).
12. Hayward, K. S., Hawkins, R., Cox, S. F. & Le Losq, C. Rheological controls on asperity weakening during earthquake slip. *J. Geophys. Res. Solid Earth* **124**, 12736–12762 (2019).
13. Rice, J. R. Heating and weakening of faults during earthquake slip. *J. Geophys. Res. Solid Earth* **111**, B05311 (2006).
14. Viesca, R. C. & Garagash, D. I. Ubiquitous weakening of faults due to thermal pressurization. *Nat. Geosci.* **8**, 875–879 (2015).
15. Reches, Z. & Lockner, D. A. Fault weakening and earthquake instability by powder lubrication. *Nature* **467**, 452–455 (2010).
16. Han, R., Hirose, T. & Shimamoto, T. Strong velocity weakening and powder lubrication of simulated carbonate faults at seismic slip rates. *J. Geophys. Res. Solid Earth* **115**, B03412 (2010).
17. Di Toro, G., Goldsby, D. L. & Tullis, T. E. Friction falls towards zero in quartz rock as slip velocity approaches seismic rates. *Nature* **427**, 436–439 (2004).
18. Sulem, J. & Famin, V. Thermal decomposition of carbonates in fault zones: slip-weakening and temperature-limiting effects. *J. Geophys. Res.* **114**, B03309 (2009).
19. Green, H. W., Shi, F., Bozhilov, K., Xia, G. & Reches, Z. Phase transformation and nanometric flow cause extreme weakening during fault slip. *Nat. Geosci.* **8**, 448–489 (2015).
20. De Paola, N., Holdsworth, R. E., Viti, C., Collettini, C. & Bullock, R. Can grain size sensitive flow lubricate faults during the initial stages of earthquake propagation? *Earth Planet. Sci. Lett.* **431**, 48–58 (2015).
21. Pozzi, G., De Paola, N., Nielsen, S. B., Holdsworth, R. E. & Bowen, L. A new interpretation for the nature and significance of mirror-like surfaces in experimental carbonate-hosted seismic faults. *Geology* **46**, 583–586 (2018).
22. Pozzi, G. et al. Coseismic ultramylonites: an investigation of nanoscale viscous flow and fault weakening during seismic slip. *Earth Planet. Sci. Lett.* **516**, 164–175 (2019).
23. Nielsen, S., Di Toro, G., Hirose, T. & Shimamoto, T. Frictional melt and seismic slip. *J. Geophys. Res. Solid Earth* **113**, B01308 (2008).
24. De Paola, N. et al. Fault lubrication and earthquake propagation in thermally unstable rocks. *Geology* **39**, 35–38 (2011).
25. De Paola, N. et al. The geochemical signature caused by earthquake propagation in carbonate-hosted faults. *Earth Planet. Sci. Lett.* **310**, 225–232 (2011).
26. De Paola, N., Faulkner, D. R. & Collettini, C. Brittle versus ductile deformation as the main control on the transport properties of low-porosity anhydrite rocks. *J. Geophys. Res.* **114**, B06211 (2009).
27. Buijze, L., Niemeijer, A. R., Han, R., Shimamoto, T. & Spiers, C. J. Friction properties and deformation mechanisms of halite(-mica) gouges from low to high sliding velocities. *Earth Planet. Sci. Lett.* **458**, 107–119 (2017).
28. Thieme, M., Demouchy, S., Mainprice, D., Barou, F. & Cordier, P. Stress evolution and associated microstructure during transient creep of olivine at 1000–1200 °C. *Phys. Earth Planet. Inter.* **278**, 34–46 (2018).
29. Gasc, J., Demouchy, S., Barou, F., Koizumi, S. & Cordier, P. Creep mechanisms in the lithospheric mantle inferred from deformation of iron-free forsterite aggregates at 900–1200 °C. *Tectonophysics* **761**, 16–30 (2019).
30. Sibson, R. H. Fault rocks and fault mechanisms. *J. Geol. Soc. Lond.* **133**, 191–213 (1977).
31. Brantut, N. & Platt, J. D. in *Fault Zone Dynamic Processes: Evolution of Fault Properties During Seismic Rupture* (eds Thomas, M. Y. et al.) 171–194 (AGU, 2017); https://doi.org/10.1002/9781119156895.ch9

32. Ashby, M. F. & Verrall, R. A. Diffusion-accommodated flow and superplasticity. *Acta Metall.* **21**, 149–163 (1973).
33. Dygert, N., Bernard, R. E. & Behr, W. M. Great basin mantle xenoliths record active lithospheric downwelling beneath central Nevada. *Geochem. Geophys. Geosyst.* **20**, 751–772 (2019).
34. Wheeler, J. Anisotropic rheology during grain boundary diffusion creep and its relation to grain rotation, grain boundary sliding and superplasticity. *Philos. Mag.* **90**, 2841–2864 (2010).
35. Miyazaki, T., Sueyoshi, K. & Hiraga, T. Olivine crystals align during diffusion creep of Earth's upper mantle. *Nature* **502**, 321–326 (2013).
36. Poirier, J.-P. *Creep of Crystals. High-Temperature Deformation Processes in Metals, Ceramics and Minerals* (Cambridge Univ. Press, 1985); https://doi.org/10.1007/978-0-387-09751-0_26
37. Barnhoorn, A., Bystricky, M., Burlini, L. & Kunze, K. The role of recrystallisation on the deformation behaviour of calcite rocks: large strain torsion experiments on Carrara marble. *J. Struct. Geol.* **26**, 885–903 (2004).
38. De Bresser, J. H. P., Ter Heege, J. H. & Spiers, C. J. Grain size reduction by dynamic recrystallization: can it result in major rheological weakening? *Int. J. Earth Sci.* **90**, 28–45 (2001).
39. Kohlstedt, D. L. in *Treatise on Geophysics* Vol. 2 (ed. Price, G. D.) 389–417 (Elsevier, 2007).
40. Mackwell, S. J. & Paterson, M. S. New developments in deformation studies: high-strain deformation. *Rev. Mineral. Geochem.* **51**, 1–19 (2002).
41. Frost, H. J. & Ashby, M. F. *Deformation-Mechanism Maps: The Plasticity and Creep of Metals and Ceramics* (Pergamon Press, 1982).
42. Schmid, S. M., Boland, J. N. & Paterson, M. S. Superplastic flow in finegrained limestone. *Tectonophysics* **43**, 257–291 (1977).
43. Pieri, M., Burlini, L., Kunze, K., Stretton, I. & Olgaard, D. L. Rheological and microstructural evolution of Carrara marble with high shear strain: results from high temperature torsion experiments. *J. Struct. Geol.* **23**, 1393–1413 (2001).
44. Wang, Q. Homologous temperature of olivine: implications for creep of the upper mantle and fabric transitions in olivine. *Sci. China Earth Sci.* **59**, 1138–1156 (2016).
45. Handy, M. R. The energetics of steady state heterogeneous shear in mylonitic rock. *Mater. Sci. Eng. A* **175**, 261–272 (1994).
46. Philpotts, A. R., Anthony R. & Ague, J. J. *Principles of Igneous and Metamorphic Petrology* (Cambridge Univ. Press, 2009).

## Methods

**Apparatus and sample assembly.** The frictional properties of rock powders were tested using a low- to high-velocity rotary shear apparatus (model MIS-233-1-77, Marui & Co.). This machine simulates the development of a narrow-fault PSZ at shallow crustal conditions (up to ~2 km in depth). Due to the rotary configuration of the apparatus, it is possible to perform experiments with an arbitrary amount of slip.

The apparatus is housed in a rigid loading frame of steel plates arranged in a vertical configuration and is composed of two vertical shafts on which the sample assembly is mounted. The upper shaft is connected through a gearbox to an electric servo-controlled motor (11 kW), which outputs a maximum rated torque of 70 Nm and maximum revolution rate of 1,500 rpm. The revolution rate and the cumulative rotation angle are measured by a tachometer and a pulse counter (3,600 pulses per full rotation), respectively, mounted on the upper shaft. The apparatus can accelerate to the maximum revolution rate (1,500 rpm) in 0.277–0.351 s at normal stresses of 25 MPa, depending on the tested material (the numbers refer to calcite and olivine powders, respectively). The axial load is applied to the lower main shaft by a pneumatic piston (Bellofram type cylinder) with an 82 mm stroke and maximum thrust of 10 kN. The axial load system is equipped with a high-precision air regulator to automatically correct the load fluctuation during the experiment. Axial load is measured using a compression load cell with a rated output of 2 mV/V ± 0.5% and resolution of ±5 kN.

The axial displacement values are measured using a high-sensitivity displacement gauge (strain gauge type) with a capacity of 10 mm and rated output of 5 mV/V ± 0.1%. Axial displacement resolution is ±2 µm. Torque values are measured by two compression load cells (strain gauge type), which are activated by a torque bar fixed to the lower shaft. The load cell capacity is 1 kN, with a rated output of 2 mV/V ± 0.5%. Torque cell resolution is ±0.5 N.

The sample assembly consists of two hollow cylinders (external radius of 12.5 mm and internal radius of 5.25 mm) sandwiching a layer of gouge (1 g, grain size 63–90 µm). The cylinders are made of titanium–vanadium alloy (Ti90Al6V4[47]), which is chosen as it has similar thermal properties (thermal conductivity of 5.8 $Wm^{-1}K^{-1}$) to common rocks. The base of each cylinder that is in contact with the gouge layer is machined with a crosshatch pattern of grooves (500 µm deep) to force shear localization within the gouge layer. A Teflon cylinder and a Teflon ring tightly fastened by a hose clip are mounted to prevent the internal and lateral extrusion of the gouge, respectively, during the experiments.

Given the cylindrical shape of the stainless steel cylinders, the slip rate ($v$) is variable across the sample. A reference radius of 8.33 mm is chosen to calculate slip and tangential slip rate of the material. The temperature rise is calculated using a simple mono-dimensional equation for heat diffusion[13] in non-adiabatic conditions (see Supplementary Section V for a detailed overview):

$$\Delta T = \frac{1}{2\rho c_P \sqrt{\pi\kappa}} \int_0^t \frac{\tau_v(t')\, v(t')}{\sqrt{t - t'}}\, dt' \quad (4)$$

where $\tau_v$ is the shear stress, $v$ is the velocity, $\rho$ is the rock density, $c_p$ is the specific heat, $\kappa$ is the thermal diffusivity, $\Phi$ is the heat flux and $t$ is time.

**Microstructural analysis.** Samples are carefully recovered after each run and prepared for microstructural analysis (see Supplementary Section I for further information). Cross sections were studied using a FEI Helios Dual Beam Nanolab 600 scanning electron microscope (SEM) at the Department of Physics of Durham. Images were acquired in backscattered (BS) and forescattered (FS) modes. BS is operated using the through-the-lens acquisition system on samples coated with graphite (<30 nm). FS is operated on uncoated specimens tilted at 70° using a 4 Quadrant KE Development FS imaging control detector. FS technique is best used for detailed microstructures as it produces good contrast along the grain boundaries.

FEI SEM was also used to prepare thin foils—carved with ion milling from specific locations of SEM-prepared samples—for transmission electron microscopy. Images were acquired on a JEOL 2100F FEG transmission electron microscope at the Department of Physics of Durham using scanning mode.

## Data availability

The mechanical data used for Figs. 1 and 4 are archived on Zenodo at https://doi.org/10.5281/zenodo.4639947. All data are available from the authors on request. Source data are provided with this paper.

## References

47. Yao, L., Ma, S., Platt, J. D., Niemeijer, A. R. & Shimamoto, T. The crucial role of temperature in high-velocity weakening of faults: experiments on gouge using host blocks with different thermal conductivities. *Geology* **44**, 63–66 (2016).

## Acknowledgements

We thank B. Mendis, L. Bowen and F. Barou for their assistance with the acquisition of SEM and TEM images and discussion, and A. Beeby for acquiring Raman spectra on our samples. This project has received funding from the European Union's Horizon 2020 research and innovation programme under the Marie Sklodowska-Curie grant agreement no. 642029 - ITN CREEP to N.D.P. and the Natural Environment Research Council (NERC) through a NERC standard grant NE/H021744/1 to N.D.P.

## Author contributions

G.P. ran the experiments and carried out the microstructural analysis and interpretations. G.P., N.D.P., S.B.N., R.E.H. and T.T. contributed equally to the concept development and to the writing of the paper. All authors jointly supervised this work.

## Competing interests

The authors declare no competing interests.

## Additional information

**Supplementary information** The online version contains supplementary material available at https://doi.org/10.1038/s41561-021-00747-8.

**Correspondence and requests for materials** should be addressed to G.P. or N.D.P.

**Peer review information** *Nature Geoscience* thanks Stephen F. Cox and the other, anonymous, reviewer(s) for their contribution to the peer review of this work. Primary Handling Editor: Stefan Lachowycz.